

The **next generation** GBCA
from Guerbet is here

Explore new possibilities >

Guerbet | 

© Guerbet 2024 GUOB220151-A

AJNR

Artificial Intelligence–Based 3D Angiography for Visualization of Complex Cerebrovascular Pathologies

S. Lang, P. Hoelter, M. Schmidt, C. Strother, C. Kaethner,
M. Kowarschik and A. Doerfler

This information is current as
of March 20, 2024.

AJNR Am J Neuroradiol 2021, 42 (10) 1762-1768

doi: <https://doi.org/10.3174/ajnr.A7252>

<http://www.ajnr.org/content/42/10/1762>

Artificial Intelligence–Based 3D Angiography for Visualization of Complex Cerebrovascular Pathologies

 S. Lang,  P. Hoelter,  M. Schmidt,  C. Strother,  C. Kaethner,  M. Kowarschik, and  A. Doerfler

ABSTRACT

BACKGROUND AND PURPOSE: By means of artificial intelligence, 3D angiography is a novel postprocessing method for 3D imaging of cerebral vessels. Because 3D angiography does not require a mask run like the current standard 3D-DSA, it potentially offers a considerable reduction of the patient radiation dose. Our aim was an assessment of the diagnostic value of 3D angiography for visualization of cerebrovascular pathologies.

MATERIALS AND METHODS: 3D-DSA data sets of cerebral aneurysms ($n_{CA} = 10$), AVMs ($n_{AVM} = 10$), and dural arteriovenous fistulas (dAVFs) ($n_{dAVF} = 10$) were reconstructed using both conventional and prototype software. Corresponding reconstructions have been analyzed by 2 neuroradiologists in a consensus reading in terms of image quality, injection vessel diameters (vessel diameter [VD] 1/2), vessel geometry index (VGI = $VD1/VD2$), and specific qualitative/quantitative parameters of AVMs (eg, location, nidus size, feeder, associated aneurysms, drainage, Spetzler-Martin score), dAVFs (eg, fistulous point, main feeder, diameter of the main feeder, drainage), and cerebral aneurysms (location, neck, size).

RESULTS: In total, 60 volumes have been successfully reconstructed with equivalent image quality. The specific qualitative/quantitative assessment of 3D angiography revealed nearly complete accordance with 3D-DSA in AVMs (eg, mean nidus size_{3D angiography/3D-DSA} = 19.9 [SD, 10.9]/20.2 [SD, 11.2] mm; $r = 0.9$, $P = .001$), dAVFs (eg, mean diameter of the main feeder_{3D angiography/3D-DSA} = 2.04 [SD, 0.65]/2.05 [SD, 0.63] mm; $r = 0.9$, $P = .001$), and cerebral aneurysms (eg, mean size_{3D angiography/3D-DSA} = 5.17 [SD, 3.4]/5.12 [SD, 3.3] mm; $r = 0.9$, $P = .001$). Assessment of the geometry of the injection vessel in 3D angiography data sets did not differ significantly from that of 3D-DSA (vessel geometry index_{AVM}: $r = 0.84$, $P = .003$; vessel geometry index_{dAVF}: $r = 0.82$, $P = .003$; vessel geometry index_{CA}: $r = 0.84$, $P < .001$).

CONCLUSIONS: In this study, the artificial intelligence–based 3D angiography was a reliable method for visualization of complex cerebrovascular pathologies and showed results comparable with those of 3D-DSA. Thus, 3D angiography is a promising postprocessing method that provides a significant reduction of the patient radiation dose

ABBREVIATIONS: AI = artificial intelligence; CA = cerebral aneurysm; dAVF = dural arteriovenous fistula; 3DA = 3D angiography; 3D-DSA = 3D digital subtraction angiography; VD = vessel diameter; VGI = vessel geometry index; VRT = volume rendering technique

DSA is the current criterion standard for diagnostics of the cerebral vasculature by acquisition of time-resolved 2D-DSA series and 3D rotational angiography (3DRA).^{1–3} Especially for the

assessment of complex vascular anatomy, 3D-DSA improves understanding of pathologies and their spatial relationship to adjacent vascular structures.⁴ Thus, 3D imaging has become an irreplaceable element in the diagnostic work-up of cerebrovascular pathologies such as cerebral aneurysms (CAs), AVMs, and dural arteriovenous fistulas (dAVFs).^{5–8}

Like conventional 2D-DSA series, 3D-DSA is based on the subtraction of a non-contrast-enhanced mask volume (mask run) from a contrast-enhanced volume (fill run), thereby allowing separation of vascular from nonvascular structures. The effective patient dose for a noncollimated 3D-DSA acquisition is 0.9 mSv.⁹ Of this amount, the mask run accounts for about 50% of the total radiation dose for both patients and investigators.¹⁰ Hence, a reduction of the radiation dose required for 3D imaging of cerebral vessels is highly desirable.

Received May 25, 2020; accepted after revision May 27, 2021.

From the Department of Neuroradiology (S.L., P.H., M.S., A.D.), University of Erlangen-Nuremberg, Erlangen, Germany; Department of Radiology (C.S.), University of Wisconsin School of Medicine and Public Health, E3/366 Clinical Sciences Center, Madison, Wisconsin; and Advanced Therapies (C.K., M.K.), Siemens Healthcare GmbH, Forchheim, Germany.

The Department of Neuroradiology, University of Erlangen-Nuremberg has a research agreement with Siemens Healthcare GmbH, Forchheim, Germany.

Disclaimer: The concepts and results presented in this paper are based on research and are not commercially available.

Please address correspondence to Stefan Lang, MD, Department of Neuroradiology, University of Erlangen-Nuremberg, Schwabachanlage 6, 91054 Erlangen, Germany; e-mail: Stefan.Lang3@uk-erlangen.de
<http://dx.doi.org/10.3174/ajnr.A7252>

There are already, however, valuable considerations for dose reduction, for example varying the scanning parameters (eg, scaling down the dose per frame) for acquisition of both mask and fill runs^{11,12} or even removing the mask run and separating opacified vascular structures from soft tissue by adjusting thresholds of the contrast-enhanced 3D data set (3DRA).¹³⁻¹⁵ While a variation of sensitive scanning parameters seems to be limited in terms of a reliable reproduction of vessels, 3DRA based on thresholding provides sufficient quality for evaluation of CAs. However, visualization of small vessels with 3DRA highly depends on the homogeneity of the applied contrast medium bolus and is thus highly susceptible to windowing.¹⁶

Recently, interesting approaches for dose-optimized 3D-DSA imaging of the cerebral vasculature have been proposed. Novel postprocessing techniques enable differentiation of vessels from adjacent structures using artificial intelligence (AI) and require only a single contrast-enhanced fill run.^{17,18} Consequently, these AI-based algorithms provide dose savings of up to 50% and might reduce a potential decrease in image quality caused by motion artifacts due to their immunity to misregistration.¹³ From a technical perspective, precise classification of different types of tissue is of central importance for these AI-based algorithms, whereby algorithms with differentiation of 3 types of tissue such as vasculature versus bone versus soft tissue¹⁷ and 2 types of tissue such as vasculature versus nonvasculature¹⁸ have been reported, respectively. Despite different classification strategies, both algorithms have shown promising results for generating DSA-like 3DA with diagnostic quality in preliminary assessments.

So far, these AI-based algorithms have been exclusively evaluated using data sets either with CAs or without pathologic findings. However, the diagnostic relevance of 3D-DSA applications is the highest in complex vascular pathologies like AVMs and dAVFs because 2D-DSA frequently has vascular overlap in these cases.

Hence, we present our experience with an AI-based 3DA prototype by means of a case series of CAs, AVMs, and dAVFs. In particular, our aim was to compare this prototypical 3DA technique classifying 2 types of tissue (vasculature versus nonvasculature) with the current standard 3D-DSA in terms of quantitative and qualitative parameters.

MATERIALS AND METHODS

Patient Selection

In a retrospective analysis, 3D-DSA data sets from 28 patients (age_{mean} = 58.7 [SD, 12.56] years; $n_{\text{female/male}}$ = 11:17) with unruptured AVMs (n_{AVM} = 10), unruptured CAs (n_{CA} = 10), and dural arteriovenous fistulas (n_{dAVF} = 10) were evaluated. All data sets were acquired before treatment of the underlying condition in the ICA in 17 cases (57%), the vertebral artery in 9 cases (30%), and the external carotid artery in 4 cases (13%). Informed consent was obtained from all patients enrolled.

3D Angiography

The prototypical 3D angiography (3DA) refers to a novel postprocessing approach with the aim of generating DSA-like 3D volumes with diagnostic image quality. In contrast to 3D-DSA, the AI-based 3DA requires only a single contrast-enhanced run (fill run) to differentiate vessels from adjacent structures.

From a technical perspective, the core of the 3DA technique can be seen as a 3D segmentation task and is based on a classification of contrast-enhanced vascular and nonvascular structures in fill run data by applying a deep convolutional neural network¹⁹ specifically trained for this task before our evaluation. In particular, the convolutional neural network is trained to determine a 3D binary segmentation mask on the basis of the fill run data, which can, in turn, be applied to the fill run data to generate a DSA-like 3D volume. The chosen network architecture is conceived as a fast 3D network with a small memory footprint. Thus, a feed-forward 3D convolutional neural network using rectified linear unit activations normalized through batch normalization²⁰ was selected. Due to the binary nature of the classification task (ie, distinguishing vascular and nonvascular structures), the binary cross-entropy was set as a loss function. The optimization is based on the Adam optimization approach,²¹ an extension of the classic stochastic gradient descent, using a batch size of 64. The base learning rate was set to 0.01. To incorporate not only local but also surrounding contextual information into the classification, we used dilated convolutions.

Analogous to an application in 1D scenarios such as generating audio waveforms (as proposed in van den Oord et al²²), the concept of dilated convolutions can be applied to multidimensional application scenarios²³ as well. The network features 4 convolutional layers with 8 filters each, a kernel size of $5 \times 5 \times 5$ voxels, and a dilation rate of 2. The final layer features a kernel size of $3 \times 3 \times 3$ voxels with 1 result filter that constitutes the classification result. The advantage of this formulation is that the proposed algorithm is fully convolutional and allows a volume of arbitrary size (eg, $512 \times 512 \times 512$ voxels) to be used as input to the classification. Furthermore, the chosen architecture allows a reasonable trade-off, especially for larger 3D volumes between the application run time and classification quality. Key aspects of the network architecture are illustrated in Fig 1.

In total, 98 retrospectively selected 3D-DSA data sets (free from metal or motion artifacts) covering a variety of conditions (to prevent overfitting) represented the training data for the 3DA algorithm. The training process was based on the presentation of both extracted contrast-enhanced runs (fill runs) and complete 3D-DSA volumes (containing mask and fill runs) to the deep convolutional neural network, aiming at a suitable classification between contrast-enhanced vascular and nonvascular structures, ie, the segmentation of the vascular structures in a 3D volume. For each individual data set used for the training of the 3DA algorithm, vascular extraction (ie, the derivation of a 3D binary segmentation mask) was performed by thresholding the subtracted 3D-DSA volumes. To determine a reasonable threshold, we considered the filling of the vasculature as well as the exclusion of undesirable influences (such as inconsistencies, image artifacts, noise, and so forth). To cover a sufficient variety of potentially suitable thresholds (eg, comparable with the personal preferences of multiple different clinical experts for a specific volume), we also included multiple thresholding choices simultaneously in the training process. Finally, this form of augmentation is intended to provide a better overall performance of the 3DA algorithm.

For the classification, randomly selected patches with a size of $31 \times 31 \times 31$ voxels were applied from the presented 3D volumes

Input 512x512x512	
Conv3D	
Kernel size (x,y,z):	5,5,5
Dilation rate (x,y,z):	1,1,1
Filters:	8
Activation:	ReLu
Conv3D	
Kernel size (x,y,z):	5,5,5
Dilation rate (x,y,z):	2,2,2
Filters:	8
Activation:	ReLu
Conv3D	
Kernel size (x,y,z):	5,5,5
Dilation rate (x,y,z):	2,2,2
Filters:	8
Activation:	ReLu
Conv3D	
Kernel size (x,y,z):	3,3,3
Dilation rate (x,y,z):	1,1,1
Filters:	1
Output 512x512x512	

FIG 1. Key aspects of the chosen network architecture. In addition to the in- and output of the network, kernel sizes, dilation rates, number of filters, and activation function (ie, rectified linear unit [ReLu]) are shown. Conv3D indicates 3D convolutional neural network.

during the training. The chosen size of the patches is the minimum input size for the network and results in a single-voxel response. The motivation for this choice was to foster randomness during the training, which, in turn, can contribute to the robustness and quality of the resulting classifier. All parameters were determined using hyperparameter tuning. Note that during the application of the prototypical 3DA method, the processing was not patch-based but was performed on an entire volume data set. Subsequent multimodal testing and validation of the prototypical algorithm of this classification were performed with separate 3D-DSA data sets. No data set of the training or validation was part of our series for evaluation of 3DA in cases of AVMs, CAs, and dAVFs.

Data Acquisition and Postprocessing

3D-DSA was acquired using a biplane flat panel detector angiographic system (Artis zee biplane; Siemens). By means of standard angiographic methods, a 5F catheter was positioned in the proximal ICA, external carotid artery, or vertebral artery to obtain 3D-DSA data sets using the standard acquisition protocol (5-second 3D-DSA) as provided by the manufacturer. Here, an initial rotational scan (native mask run) is followed by a second rotational scan (contrast-enhanced fill run) of 5 seconds each. Each run yields 133 projections (rotational angle = 200°). The detector dose per projection image is selected as 0.36 μ Gy (70 kV, 1240 \times 960 detector elements with 2 \times 2 binning of pixels, projection on a 30 \times 40 cm flat panel size, with increment of 1.5°/frame, a frame-rate of 30 frames/s). According to our protocol, a manual injection of contrast was initiated 1 second before the beginning of the fill run, maintained for 6 seconds, and stopped after the C-arm system had covered the complete rotation angle. The total contrast volume was 15 mL of Imeron 300 (iopamidol; Bracco).

Both mask and fill runs of the acquired 3D-DSA data sets were transferred to a dedicated workstation (syngo X Workplace; Siemens) running both commercially available software for conventional 3D-DSA postprocessing and an additional software prototype plug-in for the 3DA postprocessing. Reconstruction of the 3D-DSA volumes was performed using data derived from both runs, whereas reconstruction of 3DA volumes was accomplished using only data from the fill runs.

According to standardization, we used conventional reconstruction parameters for both 3DA and 3D-DSA (kernel type: edge-enhanced; characteristics: smooth; 512 \times 512 image matrix).

Image Evaluation

The image quality of all data sets was evaluated for parameters that could compromise the diagnostic value using a 5-fold grading-scale (Table 1). The 3D-DSA and 3DA reconstructions were assessed in a consensus reading by 2 experienced neuroradiologists (6 and 10 years of clinical experience) blinded to the type of reconstruction (based on either the subtraction technique or the AI algorithm).

Table 1: Image quality

Grade	Characteristics
4	Excellent (high contrast, no artifacts)
3	Good (high contrast; minimal artifacts, eg, due to movement or implants)
2	Compromised (eg, noticeable movement artifacts and/or reduced homogeneity of the vessel contrast)
1	Heavily compromised (low contrast and/or strong movement artifacts)
0	Not diagnostic (vasculature is not differentiable due to heavy artifacts and/or missing contrast)

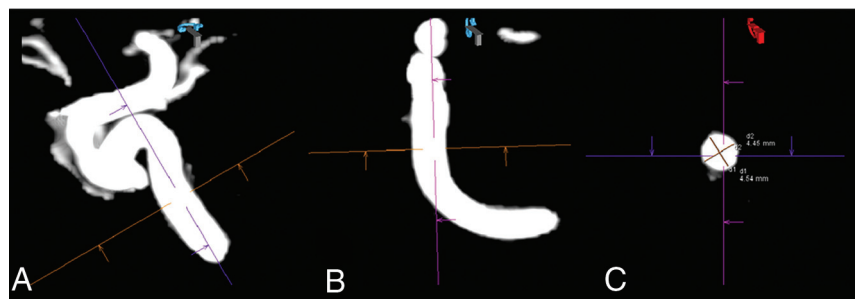


FIG 2. Sample measurement of the vascular dimensions of an ICA (C4 segment) in a 3D-DSA data set. The maximum vessel diameters have been assessed for both 3D-DSA and 3DA in 2 projections each (VD1 and VD2) using multiplanar reconstructions. A, Sagittal orientation of the C4 segment. B, Coronal orientation of the C4 segment. C, Finally, both vessel diameters allow the calculation of the VGI ($VGI = VD1/VD2$).

Assessment of 3DA and 3D-DSA Reconstructions

Vessel Geometry Index. For all 3DA- and 3D-DSA data sets, the maximum transversal diameters of the injection vessels (in millimeters; vessel diameter [VD]1/VD2) were measured in multiplanar reconstructions. Respecting the three-dimensionality of these data sets, the ratio of VD1 and VD2 was defined as the vessel geometry index ($VGI = VD1/VD2$).¹⁸ Measurements of the anterior and posterior circulation were performed at the C4 segment of the ICA and the V4 segment of the vertebral artery, respectively. If branches of the external carotid artery were involved, the maximum transversal diameter of the proximal external carotid artery was measured. See Fig 2 for an illustrative measurement of VD1 and VD2 at the ICA.

AVMs. The degree of agreement between the 3DA and 3D-DSA data sets of the AVMs was evaluated with a combination of MPR/MIP/VRT images from both types of reconstructions. As qualitative parameters, involvement of eloquent brain areas, origin of the main feeder, venous drainage (superficial, deep, mixed), and the presence of venous varix or stenosis were determined. Moreover, the number of feeders, the presence and number of aneurysms on feeding arteries, the number of intranidal aneurysms, and the maximum diameter of the nidus were determined as quantitative parameters. On the basis of these data, Spetzler-Martin scores were also determined.

dAVFs. The degree of agreement between the 3DA and 3D-DSA data sets of the dAVFs was also evaluated with a combination of MPR/MIP/VRT images from both types of reconstructions. As qualitative parameters, the origin of the main feeder (eg, middle/posterior meningeal artery, ophthalmic artery, ascending pharyngeal

artery), the localization of the fistulous point (anterior/middle/posterior cranial fossa), the primary vessel of venous drainage (vein or sinus), and drainage of the fistula into a dural sinus (transverse sigmoid, petrous, superior sagittal, and straight sinuses) were recorded. As a quantitative parameter, the maximum diameter of the main feeder was also obtained.

CAs. The degree of agreement between the 3DA and 3D-DSA data sets of the CAs was also evaluated with a combination of MPR/MIP/VRT images from both types of reconstructions. As qualitative parameters, the localization (parent artery) of the aneurysm and its neck configuration were recorded. As quantitative parameters, the maximum diameter of aneurysmal sac and the number of aneurysmal blebs were also noted.

Statistical Analysis

Statistical analysis was performed using commercially available software (SPSS Statistics, Version 20; IBM).

Because of their noncontinuous character, qualitative parameters (eg, location of the pathology and so forth) were analyzed using descriptive statistics.

Quantitative parameters from both groups (eg, vessel diameters, VGIs, diameter of the AVM nidus, diameter of the main dAVF feeder, and diameter of aneurysmal sac) were tested for normal distribution using the D'Agostino-Pearson test (if $P > .05$, normality was accepted) and were compared using the Pearson correlation coefficient (r) and a paired t test (P), respectively. Any other quantitative parameters (eg, number of AVM feeders, aneurysms on AVM feeding arteries, number of intranidal aneurysms, number of aneurysmal blebs, and so forth) were analyzed using descriptive statistics.

RESULTS

Image Quality

The 3DA and 3D-DSA reconstructions ($n = 60$), respectively, were all of diagnostic quality with a low number of cases with reduced image quality due to motion artifacts (3DA: $n_{\text{excellent}} = 23$, $n_{\text{good}} = 7$; 3D-DSA: $n_{\text{excellent}} = 23$, $n_{\text{good}} = 7$).

Qualitative and Quantitative Assessment of 3D-DSA and 3DA Reconstructions

VGI. In all 3DA and 3D-DSA reconstructions, measurement of vessel diameters was successfully performed ($n_{3DA} = 60$, $n_{3D-DSA} = 60$), and the acquired values for AVMs, dAVFs, and CAs did not show significant differences. Concordantly, the corresponding VGIs did not differ significantly as well. See Table 2 for details.

Table 2: VD and VGI

Parameter	3DA (Mean)	3D-DSA (Mean)	<i>r</i>	<i>P</i>
VD1 _{AVM}	3.82 (SD, 0.47) mm	3.81 (SD, 0.55) mm	0.988	<.001
VD2 _{AVM}	3.97 (SD, 0.60) mm	3.94 (SD, 0.59) mm	0.984	<.001
VGI _{AVM}	0.96 (SD, 0.04) mm	0.97 (SD, 0.03) mm	0.835	.003
VD1 _{CA}	4.39 (SD, 0.84) mm	4.34 (SD, 0.87) mm	0.998	<.001
VD2 _{CA}	4.61 (SD, 0.81) mm	4.54 (SD, 0.85) mm	0.996	<.001
VGI _{CA}	0.95 (SD, 0.04) mm	0.95 (SD, 0.03) mm	0.955	<.001
VD1 _{dAVF}	4.24 (SD, 0.72) mm	4.22 (SD, 0.77) mm	0.993	<.001
VD2 _{dAVF}	4.44 (SD, 0.780) mm	4.43 (SD, 0.81) mm	0.992	<.001
VGI _{dAVF}	0.95 (SD, 0.02) mm	0.95 (SD, 0.02) mm	0.824	.003



FIG 3. Illustrative case 1. Sample visualization of a right-sided AVM with 3D-DSA (A) and the AI-based 3DA (B) using VRT. 3DA (B) shows both feeding arteries originating from the MCA and the nidus and drainage via superficial veins, equivalent to 3D-DSA. Not only the flow-associated aneurysm of the MCA bifurcation (red arrow) but also the venous ectasia adjacent to the nidus is comparably visualized without loss of information using 3DA.

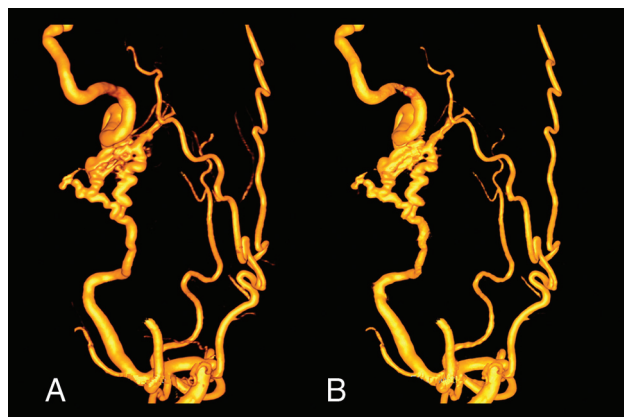


FIG 4. Illustrative case 2. Sample visualization of a left-sided dAVF with 3D-DSA (A) and the AI-based 3DA (B) using VRT. 3DA (B) offers comparable visualization of the influx of the fistula via the dilated middle meningeal artery and the drainage of the fistula via an ectatic cerebral vein compared with 3D-DSA (A).

AVMs. In total, 10 data sets acquired via the ICA ($n_{\text{right}} = 4$, $n_{\text{left}} = 1$) and vertebral artery ($n_{\text{right}} = 3$, $n_{\text{left}} = 2$) and having 10 AVMs were successfully postprocessed and evaluated. Qualitative

assessment of the corresponding 3DA and 3D-DSA data sets revealed identical results concerning the involvement of eloquent brain areas ($n_{3\text{DA}/3\text{D-DSA}} = 8$), origin of the main feeder (3DA/3D-DSA: $n_{\text{posterior cerebral artery}} = 6$, $n_{\text{MCA}} = 3$, $n_{\text{anterior cerebral artery}} = 1$), and drainage (3DA/3D-DSA: $n_{\text{superficial}} = 4$, $n_{\text{deep}} = 4$, $n_{\text{mixed}} = 2$) and pathologies of venous vessels (3DA/3D-DSA: $n_{\text{venous pouch}} = 4$). The number of arterial feeders ($n_{3\text{DA}/3\text{D-DSA}} = 16$) and associ-

ated flow-related ($n_{3\text{DA}/3\text{D-DSA}} = 3$) and intranidal aneurysms ($n_{3\text{DA}/3\text{D-DSA}} = 3$) was rated identically for both modalities. Measurement of the nidus size in 3DA reconstructions (mean, 19.9 [SD, 10.9] mm) showed a strong correlation ($r = 0.9/P = .001$) to 3D-DSA (mean, 20.2 [SD, 11.2] mm). The Spetzler-Martin score was rated identically for AVMs in 3DA and 3D-DSA reconstructions (3DA/3D-DSA: $n_{\text{Spetzler-Martin score 1}} = 1$, $n_{\text{Spetzler-Martin score 2}} = 4$, $n_{\text{Spetzler-Martin score 3}} = 5$). For an illustrative case see Fig 3.

dAVFs. In total, 10 data sets, acquired via the ICA ($n_{\text{right}} = 2$, $n_{\text{left}} = 1$), external carotid artery ($n_{\text{right}} = 2$, $n_{\text{left}} = 2$), and vertebral artery ($n_{\text{right}} = 1$, $n_{\text{left}} = 2$) with 10 dAVFs were successfully postprocessed and evaluated. Qualitative assessment of the corresponding 3DA and 3D-DSA data sets revealed identical results concerning the origin of the main feeder (3DA/3D-DSA: $n_{\text{ophthalmic artery}} = 3$, $n_{\text{middle meningeal artery}} = 3$, $n_{\text{posterior meningeal artery}} = 3$, $n_{\text{ascending pharyngeal artery}} = 1$), localization of the fistulous point (3DA/3D-DSA: $n_{\text{anterior cranial fossa}} = 2$, $n_{\text{middle cranial fossa}} = 4$, $n_{\text{posterior cranial fossa}} = 4$), primary vessel of drainage (3DA/3D-DSA: $n_{\text{vein}} = 9$, $n_{\text{sinus}} = 1$), and drainage of the fistula (3DA/3D-DSA: $n_{\text{transverse sigmoid sinus}} = 3$, $n_{\text{superior sagittal sinus}} = 3$, $n_{\text{straight sinus}} = 4$). Measurement of the maximum diameter of the main feeder in the 3DA reconstructions (mean, 2.04 [SD, 0.65] mm) showed a strong correlation ($r = 0.9/P = .001$) to 3D-DSA (mean, 2.05 [SD, 0.63] mm). For an illustrative case see Fig 4.

CAs. In total, 10 data sets, acquired via the ICA ($n_{\text{right}} = 4$, $n_{\text{left}} = 5$) and vertebral artery ($n_{\text{right}} = 1$) and having 10 CAs, were successfully postprocessed and evaluated. Qualitative assessment of the corresponding 3DA and 3D-DSA data sets revealed identical results concerning the identification of the parent vessel (3DA/3D-DSA: $n_{\text{Anterior communicating artery}} = 2$, $n_{\text{MCA}} = 4$, $n_{\text{ICA}} = 3$, $n_{\text{basilar artery}} = 1$) and the aneurysmal neck configuration (3DA/3D-DSA: $n_{\text{small}} = 3$, $n_{\text{medium}} = 2$, $n_{\text{large}} = 5$). Measurement of the maximum diameter of the aneurysmal sac in the 3DA reconstructions (mean, 5.17 [SD, 3.4] mm) showed a strong correlation ($r = 0.9/P = .001$) to 3D-DSA (mean, 5.12 [SD, 3.3] mm). The number of aneurysmal blebs was equivalent in both types of reconstructions (3DA/3D-DSA: $n = 3$). For an illustrative case see Fig 5.

DISCUSSION

3D imaging of neurovascular pathologies is invaluable in diagnostics and therapy. So far, 3D-DSA with an established acquisition protocol and efficient postprocessing is regarded as standard. Approximately 50% of the radiation dose required for a 3D-DSA



FIG 5. Illustrative case 3. Sample 3D visualization of an irregular aneurysm of the anterior communicating artery in VRT reconstructions using 3D-DSA (A) and 3DA (B). Despite differences concerning the reconstruction algorithm, AI-based 3DA (B) provides all relevant information on the aneurysmal configuration equivalent to 3D-DSA.

acquisition is necessary for acquisition of a mask; alone, the mask contains no clinically useful vascular information. Moreover, the subtraction technique is susceptible to artifacts due to misregistration of the mask and fill runs. Thus, AI-based algorithms like 3DA requiring only a single contrast-enhanced run have been developed for obtaining a maskless 3DA. This reduces the radiation dose and may also improve image quality by eliminating the eventuality of intersweep motion. Because AI-based algorithms have already been validated for vessels without pathologic findings¹⁸ and for CAs,¹⁷ the potential of this technique for generating DSA-like 3DAs with diagnostic quality has already been demonstrated. However, 3D imaging is needed most in AVMs and dAVFs. Hence, an assessment of 3DA with regard to complex pathologies is imperative before clinical implementation.

In our series, 3DA as a novel prototypical postprocessing technique was performed successfully for all data sets by differentiating 2 types of tissue (vasculature versus nonvasculature) and was suitable for visualization of CAs, AVMs, and dAVFs. When we took specific characteristics of these pathologies into account, our quantitative and qualitative analyses of 3DA demonstrated excellent agreement with standard 3D-DSA reconstructions. Even though 3DA has not left the prototype stage yet, future clinical application seems promising because no loss of information has been observed. As a result of the clinical implementation of 3DA, the effective patient dose required for 3D imaging of the cerebral vasculature would be reduced by approximately 50%: Based on usual dose values for a 3D-DSA acquisition ranging from 0.3 to 0.9 mSv (depending on the extent of collimation), 0.15–0.45 mSv per acquisition may be saved, respectively. Although an estimated dose reduction below average values of 0.35 mSv per acquisition might not substantially impact a patient's associated lifetime cancer risk, reliable dose savings would be achievable through the use of 3DA.

Previously, Montoya et al¹⁷ have demonstrated that their AI-based algorithm (3D deep learning angiography [3D-DLA]) precisely extracts the vascular anatomy in a DSA-like manner in a series of 62 data sets. The authors analyzed the quality of vessel separation from adjacent bone and soft tissue in 3D-DLA by quantitative and qualitative parameters in cases with cerebrovascular abnormalities. 3D-DLA provided a vasculature classification accuracy of 98.7%, high-quality bone removal, and reduced misregistration artifacts caused by intersweep motion. Although

the authors provided image examples of CAs, there was no statement regarding the exact composition of their patient cohort (cases were selected in a random fashion). Moreover, a dedicated assessment of CAs concerning qualitative (eg, configuration) and quantitative (eg, size) parameters has not been performed. Nevertheless, the authors demonstrated that 3D-DLA is applicable to vascular pathologies. Because the analysis of Montoya et al¹⁷ exclusively allows conclusions about CAs, our detailed evaluation covering CAs, AVMs, and dAVFs is another important component to assess the value of AI-based algorithms in this context and to prepare their future clinical implementation. However, all AI-based algorithms depend directly on the chosen network architecture. Provided that appropriate data sets (in particular 3D-DSA data sets of adequate quality) have been used for training the network, we fully agree that AI-based algorithms such as 3D-DLA or 3DA have the potential to simultaneously improve the image quality and reduce the radiation dose.

Most interesting, “simple” thresholding of a single contrast-enhanced data set is another remarkable option to generate DSA-like images for 3DRA.¹³ Similar to AI-based approaches, 3DRA is not based on the subtraction technique and does not require a mask run. Consequently, the radiation dose can be almost halved compared with 3D-DSA. Simultaneously, 3DRA does not have susceptibility for misregistration artifacts or for intersweep motion and may improve image quality. So far, 3DRA has been evaluated in cases of CAs and was a valuable method for their preinterventional assessment. Because of its accuracy in these cases, the clinical implementation of 3DRA has already been achieved. However, 3DRA is based on modifying thresholds for the contrast-enhanced 3D data to provide differentiation of vascular from nonvascular structures.¹⁴ As a consequence, poorly opacified vessels (eg, perforators) are potentially harmed by this reconstruction process and are in danger of not being visualized.¹⁶ Therefore, we must assume that in general, 3DRA is limited regarding visualization of complex arteriovenous pathologies. Nevertheless, 3DRA significantly contributes to a reduction of the radiation dose required for the diagnostic work-up of CAs. However, our results indicate that 3DA as an AI-based algorithm is not restricted in terms of visualization of the angioarchitecture of an AVM or dAVF. In fact, our experience concerning visualization of very small vessels like perforating arteries with 3DA is in complete accordance with previously published data.^{17,18} Hence, 3DA provides significant benefits because of its broad field of applications.

Also, direct manipulation of scanning parameters can be an effective concept for realizing significant dose reductions regarding 3D-DSA acquisitions. Pearl et al^{11,12} demonstrated that simple downscaling of the applied dose is not necessarily associated with poor image quality. In the end, the authors worked out a low-dose protocol that both leads to a relevant dose reduction (up to 30%) and preserves diagnostic quality of the 3D-DSA data sets. However, any manipulation of scanning parameters caused statistically significant alterations regarding the representation of the vascular geometry and is potentially associated with loss of relevant information. In the clinical routine, this inconsistency is only tolerable to a certain extent and might be disadvantageous, especially in complex cases. Nevertheless, the work of Pearl et al is highly relevant for the evolution of AI-based algorithms. As soon

as we learn to combine low-dose protocols with AI-based algorithms, we will be able to take full advantage of both dose-saving techniques. Therefore, future research should focus on the development of clinically applicable dose-reduced single-run protocols.

Limitations

Although clinically useful 3DA was achieved from all data sets, our analysis has limitations. First, it was limited by the small sample size. Moreover, our retrospective series included only preoperative/preinterventional cases of vascular pathologies; it does not address the qualification of the prototypical 3DA to visualize metallic implants (eg, embolization material). Additionally, our series did not include cases with heavily compromised image quality (eg, motion artifacts) and contrast variations (eg, data sets with varying contrast media dilutions). Nevertheless, our analysis exclusively evaluated 1 specific AI-based algorithm for vessel recreation, classifying 2 types of tissue (vasculature versus nonvasculature). Thus, the results concerning the diagnostic value of the proposed 3DA algorithm can be transferred only to other AI-based angiographic algorithms with comparable characteristics. In fact, further investigations focusing on these issues are required to assess the full clinical applicability of this new method.

CONCLUSIONS

The investigated AI-based 3DA algorithm used in cases of complex AVMs, dAVFs, and CAs and obtaining DSA-like 3D volumes provided the same utility as conventionally reconstructed 3D-DSA volumes. Moreover, because this method does not rely on the subtraction technique, AI-based 3DA offers a significant reduction of the effective patient radiation dose. Thus, the clinical implementation of this promising postprocessing algorithm should be pursued.

Disclosures: Christian Kaethner—UNRELATED: Employment: Siemens, Comments: full-time employee. Markus Kowarschik—UNRELATED: Employment: Siemens, Comments: full-time employee.

REFERENCES

- Wong SC, Nawawi O, Ramli N, et al. **Benefits of 3D rotational DSA compared with 2D DSA in the evaluation of intracranial aneurysm.** *Acad Radiol* 2012;19:701–07 Jun [CrossRef Medline](#)
- van Rooij WJ, Sprengers ME, de Gast AN, et al. **3D rotational angiography: the new gold standard in the detection of additional intracranial aneurysms.** *AJNR Am J Neuroradiol* 2008;29:976–79 [CrossRef Medline](#)
- Mistretta CA, Crummy AB, Strother CM. **Digital angiography: a perspective.** *Radiology* 1981;139:273–76 [CrossRef Medline](#)
- Hochmuth A, Spetzger U, Schumacher M. **Comparison of three-dimensional rotational angiography with digital subtraction angiography in the assessment of ruptured cerebral aneurysms.** *AJNR Am J Neuroradiol* 2002;23:1199–205 [Medline](#)
- Anxionnat R, Bracard S, Ducrocq X, et al. **Intracranial aneurysms: clinical value of 3D digital subtraction angiography in the therapeutic decision and endovascular treatment.** *Radiology* 2001;218:799–808 [CrossRef Medline](#)
- Missler U, Hundt C, Wiesmann M, et al. **Three-dimensional reconstructed rotational digital subtraction angiography in planning treatment of intracranial aneurysms.** *Eur Radiol* 2000;10:564–68 [CrossRef Medline](#)
- Ogilvy CS, Stieg PE, Awad I, et al. **Special Writing Group of the Stroke Council, American Stroke Association. AHA Scientific Statement: recommendations for the management of intracranial arteriovenous malformations—a statement for healthcare professionals from a Special Writing Group of the Stroke Council, American Stroke Association.** *Stroke* 2001;32:1458–71 [CrossRef Medline](#)
- Oppenheim C, Meder JF, Trystram D, et al. **Radiosurgery of cerebral arteriovenous malformations: is an early angiogram needed?** *AJNR Am J Neuroradiol* 1999;20:475–81 [Medline](#)
- Struffert T, Hauer M, Banckwitz R, et al. **Effective dose to patient measurements in flat-detector and multislice computed tomography: a comparison of applications in neuroradiology.** *Eur Radiol* 2014;24:1257–65 [CrossRef Medline](#)
- Kim DJ, Park MK, Jung DE, et al. **Radiation dose reduction without compromise to image quality by alterations of filtration and focal spot size in cerebral angiography.** *Korean J Radiol* 2017;18:722–28 [CrossRef Medline](#)
- Pearl MS, Torok CM, Messina SA, et al. **Reducing radiation dose while maintaining diagnostic image quality of cerebral three-dimensional digital subtraction angiography: an in vivo study in swine.** *J Neurointerv Surg* 2014;6:672–76 [CrossRef Medline](#)
- Pearl MS, Torok C, Katz Z, et al. **Diagnostic quality and accuracy of low dose 3D-DSA protocols in the evaluation of intracranial aneurysms.** *J Neurointerv Surg* 2015;7:386–90 [CrossRef Medline](#)
- Grass M, Koppe R, Klotz E, et al. **Three-dimensional reconstruction of high contrast objects using C-arm image intensifier projection data.** *Comput Med Imaging Graph* 1999;23:311–21 [CrossRef Medline](#)
- Raabe A, Beck J, Rohde S, et al. **Three-dimensional rotational angiography guidance for aneurysm surgery.** *J Neurosurg* 2006;105:406–11 [CrossRef Medline](#)
- Gosch D, Kurze W, Deckert F, et al. **Radiation exposure with 3D rotational angiography of the skull.** *Rofo* 2006;178:880–05 [CrossRef Medline](#)
- Hirai T, Korogi Y, Suginozawa K, et al. **Clinical usefulness of unsubtracted 3D digital angiography compared with rotational digital angiography in the pretreatment evaluation of intracranial aneurysms.** *AJNR Am J Neuroradiol* 2003;24:1067–74 [Medline](#)
- Montoya JC, Li Y, Strother C, et al. **3D deep learning angiography (3D-DLA) from C-arm conebeam CT.** *AJNR Am J Neuroradiol* 2018;39:916–22 [CrossRef Medline](#)
- Lang S, Hoelter P, Schmidt MA, et al. **Evaluation of an artificial intelligence-based 3D-angiography for visualization of cerebral vasculature.** *Clin Neuroradiol* 2020;30:705–12 [CrossRef Medline](#)
- Goodfellow I, Bengio Y, Courville A. *Deep Learning*. MIT Press; 2016
- Ioffe S, Szegedy C. **Batch normalization: accelerating deep network training by reducing internal covariate shift.** In: *Proceedings of the 32nd International Conference on Machine Learning*, Lille, France. July 7–11, 2015;37:448–56
- Kingma D, Ba J. **Adam: a method for stochastic optimization.** In: *Proceedings of the International Conference on Learning Representations*, San Diego, California. May 7–9, 2015
- van den Oord A, Dieleman S, Zen H, et al. **WaveNet: a generative model for raw audio.** 2016. arXiv: 1609.03499v2[cs.LG]. https://arxiv.org/abs/1609.03499?source=post_page630afcafb9dd. Accessed April 22, 2020
- Yu F, Koltun V. **Multi-scale context aggregation by dilated convolutions.** 2016. arXiv: 1511.07122v3[cs.CV]. <http://export.arxiv.org/abs/1511.07122v3>. Accessed May 8, 2020